PNAS RESEARCH ARTICLE | BIOCHEMISTRY OPEN ACCESS

Blocking C-terminal processing of KRAS4b via a direct covalent attack on the CaaX-box cysteine

Anna E. Maciag[a,1], Yue Yang[b], Alok K. Sharma[a], David M. Turner[a], Caroline J. DeHart[a], Hazem Abdelkarim[c], Lixin Fan[d], Brian P. Smith[a], Vandana Kumari[a], Marcin Dyba[a], Megan Rigby[a], Jean A. Castillo Badillo[a], Lauren Adams[e], Luca Fornelli[f], Stephen Fox[a], Alla Brafman[a], Thomas Turbyville[a], William Gillette[a], Simon Messing[a], Constance Agamasu[a], Andrew L. Wolfe[g], Stephan Gysin[g], Albert H. Chan[a], Dhirendra K. Simanshu[a], Dominic Esposito[a], Oleg Chertov[a], Andrew G. Stephen[a], Michelle Arkin[h], Adam Renslo[h], Neil L. Kelleher[i], Vadim Gaponenko[c], Felice C. Lightstone[b], Dwight V. Nissley[a], and Frank McCormick[a,g,1]

Affiliations are included on p. 9.

Contributed by Frank McCormick; received June 17, 2024; accepted April 2, 2025; reviewed by Geoffrey J. Clark and Mark R. Philips

***RAS* is the most frequently mutated oncogene in cancer. RAS proteins show high sequence similarities in their G-domains but are significantly different in their C-terminal hypervariable regions (HVR). These regions interact with the cell membrane via lipid anchors that result from posttranslational modifications (PTM) of cysteine residues. KRAS4b is unique as it has only one cysteine that undergoes PTM, C185. Small molecule covalent modification of C185 would block any form of prenylation and subsequently inhibit attachment of KRAS4b to the cell membrane, blocking its biological activity. We translated this concept to the discovery and development of disulfide tethering screen hits into irreversible covalent modifiers of C185. These compounds inhibited proliferation of KRAS4b-driven mouse embryonic fibroblasts, but not cells driven by N-myristoylated KRAS4b that harbor a C185S mutation and are not dependent on C185 prenylation. Top–down proteomics was used to confirm target engagement in cells. These compounds bind in a pocket formed when the HVR folds back between helix 3 and 4 in the G-domain (HVR-α3-α4). This interaction can happen in the absence of small molecules as predicted by molecular dynamics simulations and is stabilized in the presence of C185 binders as confirmed by small-angle X-ray scattering and solution NMR. NOESY-HSQC, an NMR approach that measures internuclear distances of 6 Å or less, and structure analysis identified the critical residues and interactions that define the HVR-α3-α4 pocket. Further development of compounds that bind to this pocket could be the basis of a new approach to targeting KRAS cancers.**

KRAS | KRAS4b | C185 | HVR | covalent inhibitor

Significance

The development of small molecule KRAS inhibitors has proven to be a challenge. Recent clinical development of covalent KRAS G12C inhibitors demonstrates the potential of targeting KRAS oncogenic proteins directly. Compounds that target the KRAS G12D allele, as well pan-RAS and pan-KRAS compounds, are also under development. Preventing plasma membrane attachment of KRAS with a small molecule covalent modifier of C185 represents an alternative approach that would lead to inhibition of all KRAS-driven tumors. We have identified compounds that dock to a pocket formed by the hypervariable regions and Helix3/Helix4 (HVR-α3-α4) in KRAS4b, and covalently modify C185 before its lipid modification occurs. This unique mechanism of KRAS inhibition offers a strong rationale for further development of this class of compounds.

KRAS is the most frequently mutated oncogene in cancer. Of the three major isoforms of *RAS* (*K*–, *H*–, and *N-RAS*), mutant KRAS proteins play a causal and leading role in three major human cancers: lung, colorectal, and pancreatic (1–3). *KRAS* produces 2 splice variants: KRAS4a and KRAS4b. KRAS4b is a highly studied protein, and is composed of a well-defined N-terminal cytoplasmic guanosine nucleotide-binding domain (G domain of ~1–169 aa) and a C-terminal flexible hypervariable region (HVR, comprising ~19 aa) that is anchored to the inner leaflet of the cell membrane (4, 5).

Canonical RAS isoforms (HRAS, KRAS4a, KRAS4b, and NRAS) share a high degree of sequence similarity within the G domain, but differ significantly in the hypervariable region (HVR), which undergoes isoform-specific posttranslational modifications (PTM). PTM at the HVR is an essential step in RAS protein trafficking and membrane localization (6, 7), and occurs as palmitoylation and/or prenylation (farnesylation or geranylgeranylation) at different cysteine residues within the HVR (8) via the attachment of hydrophobic lipid moieties, which serve as a membrane anchor (5, 9, 10). While all four RAS isoforms are prenylated at the terminal cysteine residue of the HVR CAAX motif, KRAS4b is unique in that it does not undergo palmitoylation (7). Unlike KRAS4a, HRAS, and NRAS, the HVR of KRAS4b includes a poly-lysine stretch (K175-K180) that serves as a secondary site for enhancing plasma membrane association (9).

Blocking RAS PTM and abrogating its membrane localization offers a potential approach for therapeutic intervention. Inhibitors of farnesyl transferases (FTIs) have been investigated for their potential to attenuate the c-terminal lipid modification that is required for RAS plasma membrane localization and downstream signaling pathway activation. FTIs showed high preclinical anticancer activity in tumors driven by HRAS (11). The FTI Tipifarnib is in clinical trials and appears to show activity in head and neck squamous cell carcinomas harboring oncogenic HRAS mutations. Unfortunately, this

Reviewers: G.J.C., University of Louisville; and M.R.P., New York University School of Medicine.

Competing interest statement: Reviewer M.R.P and co-author D.S. were co-authors of a review in 2023.

[1]To whom correspondence may be addressed. Email: anna.maciag@nih.gov or Frank.mccormick@ucsf.edu.

This article contains supporting information online at https://www.pnas.org/lookup/suppl/doi:10.1073/pnas.2410766122/-/DCSupplemental.

Published May 9, 2025.

approach yielded little effect against KRAS-driven cancers, as KRAS (and also NRAS) undergoes alternative prenylation (geranylgeranylation) in the presence of FTIs, and remains functionally active (12).

Covalent modification of the CaaX-box cysteine (C185) of KRAS4b would block all prenylation at that site and inhibit the subsequent attachment of the KRAS protein to the plasma membrane, which is a key step required for KRAS signaling. This approach of targeting a single protein isoform would likely yield less side effects than the global disruption of all farnesyltransferase substrates, as seen with FTIs. Covalent targeting of the C185 residue of KRAS4b was reported by Nnadi et al. in their work identifying KRAS G12C Switch-2 binders (13).

We used disulfide tethering to search for compounds that selectively modify C185 in KRAS4b. Disulfide tethering is a site-directed, fragment-based drug discovery method that allows screening of low-affinity disulfide-containing fragments against cysteine residues in a target protein (14). Fragment binding is reversible and can be tuned to favor detection of only the strongest-bound fragments using increasing concentrations of a reductant, typically β-mercaptoethanol. This binding is not purely driven by reactivity; it is also strongly dependent on protein/ligand interactions. Bound fragments are detected by mass spectrometry (MS) and provide a lead into the drug discovery process.

We applied the disulfide tethering technology to identify fragments that bind and covalently modify C185 in KRAS4b and not C186 in NRAS. The ability to identify compounds that bind to KRAS4b through covalent attachment to C185 suggests the presence of an adjacent pocket to which fragments bind noncovalently. The failure to detect compounds that bind to full-length NRAS suggests that only KRAS forms this putative pocket. By employing the powerful combination of molecular dynamics (MD) simulation, small-angle X-ray scattering (SAXS), and solution NMR spectroscopy, we elucidated the induced structural changes within the KRAS4b-compound complex that are driven by C185 modification and pocket binding.

Results

We screened the University of California San Francisco disulfide tethering library against full-length KRAS4b (aa 1–188) proteins, then counterscreened against full-length 1–189 NRAS. Fragment 6B9 (compound **1**) (Fig. 1*A*) gave the greatest degree of modification to KRAS4b (Fig. 1*A*) and did not modify NRAS. KRAS4b 1–188 that has C185 mutated to serine (C185S) did not show any modification, suggesting C185 as the sole site of modification (Fig. 1*A*). Our ability to identify compounds that bind to KRAS4b through covalent attachment to C185 indicates that there must be a pocket adjacent to C185 to which the compound binds noncovalently. Our failure to detect compounds that bind to full-length NRAS also suggests that this putative pocket is specific to KRAS4b.

Converting the Disulfide Tethering Hit to an Electrophile. Disulfides are unsuitable for use as cellular probes. Therefore, we assessed alternative electrophilic groups, and identified vinyl sulfonamide as a suitable replacement due to its moderate electrophilic activity and good stability in cells. This approach led to the discovery of compound SMDC994566 (compound **2**) (structure in Fig. 1*B*, synthesis described in *SI Appendix*). Compound **2** showed reactivity toward full-length KRAS4b in vitro through covalent modification of C185, and demonstrated single-site labeling with no modification of other known reactive residues in KRAS4b (e.g., solvent exposed C118) (Fig. 1*B*). As expected, compound **2** did not react with fully processed KRAS4b protein, in which C185 is farnesylated and the C-terminal carboxylic acid is methylated (KRAS4b FME) (15).

C185-Reactive Compounds Exhibit Inhibitory Effect in KRAS-Dependent Cells. To test the ability of C185-reactive compounds to block KRAS4b function in cells, we used a panel of mouse embryonic fibroblasts (MEF) cell lines driven by a single isoform of KRAS and lacking NRAS and HRAS (16). As a control for off-target effects, we generated a MEF cell line that is dependent on N-terminally myristoylated KRAS4b G12D/C185S, which is incapable of modification at C185 but retains the membrane localization necessary for signaling (Myr-KRAS-G12D/C185S, *SI Appendix*, Fig. S1). Compound **2** inhibited the proliferation of KRAS4b mutant MEFs but did not inhibit the growth of Myr-KRAS G12D/C185S MEFs (Fig. 1*C*). It also reduced KRAS protein levels in KRAS4b G12D and G12C but not in Myr-KRAS G12D/C185S MEFs after 72 h of treatment (Fig. 1*D*).

Next, we tested the hypothesis that C185-targeting compounds covalently modify this residue in newly synthesized KRAS, preventing its posttranslational processing and subsequent membrane attachment. HeLa cells expressing doxycycline-inducible green fluorescent protein (GFP)-tagged KRAS4b G12D or NRAS G12D were treated with the more advanced analogue of compound **2**, compound **3** (Fig. 2 *A* and *B*, structure shown in Fig. 2*C*). Localization of RAS proteins at the plasma membrane was monitored by colocalization with Concanavalin A as a membrane marker. As shown in Fig. 2*A*, treatment with 10 μM compound **3** for 24 h decreased the level of membrane-bound GFP-KRAS4b G12D, with no or minimal effect on GFP-NRAS G12D (Fig. 2*B*).

Similarly, compound **3** affected membrane localization in MEF cells expressing the G12V mutant of KRAS4b or NRAS, (Fig. 2*D*). Treatment with 20 μM compound **3** decreased the amount of KRAS4b, but not NRAS, in cellular membrane fractions (Fig. 2*D*), confirming that NRAS is not a target of these compounds. As observed in our earlier experiments with MEFs (Fig. 1*C*), reduction of KRAS4b G12V protein levels is also noticeable in cells treated with compound **3**. However, mechanisms leading to this decrease are unclear and would require further investigation.

Verification of Target Engagement. To obtain direct evidence for covalent engagement of C185 in cells, we used top–down proteomics (TDP) methodology that uses MS to analyze intact proteins and distinguish proteoform complexity (17). We treated cells with compound **3**, purified KRAS, and searched for covalently modified C185 (Fig. 2 *F–I*).

KRAS4b attachment to the membrane is facilitated by farnesylation of the C185 residue, followed by additional processing of the CAAX motif which involves cleavage of the -AAX residues by RCE1 (RAS converting CAAX endopeptidase 1) (8). Finally, the farnesylated cysteine residue is carboxymethylated by ICMT (isoprenylcysteine carboxyl methyltransferase) (18, 19). For TDP we used HEK293 cells expressing FLAG-tagged KRAS4b G12D under a doxycycline-inducible promoter. We induced this system with doxycycline for 6 h, then treated cells with compound **3** alone or in combination with L-778,123, a dual inhibitor of farnesyl transferase and geranylgeranyl transferase type I. Following FLAG purification, and then MS analysis, we detected a mass addition of 616.16 Da under both experimental conditions that corresponds to KRAS4b modified with compound **3**, lacking the farnesyl and retaining the last three amino acid residues (VIM) (Fig. 2 *C–E*), which is consistent with our hypothesis and the pattern of posttranslational KRAS4b processing. Subsequent

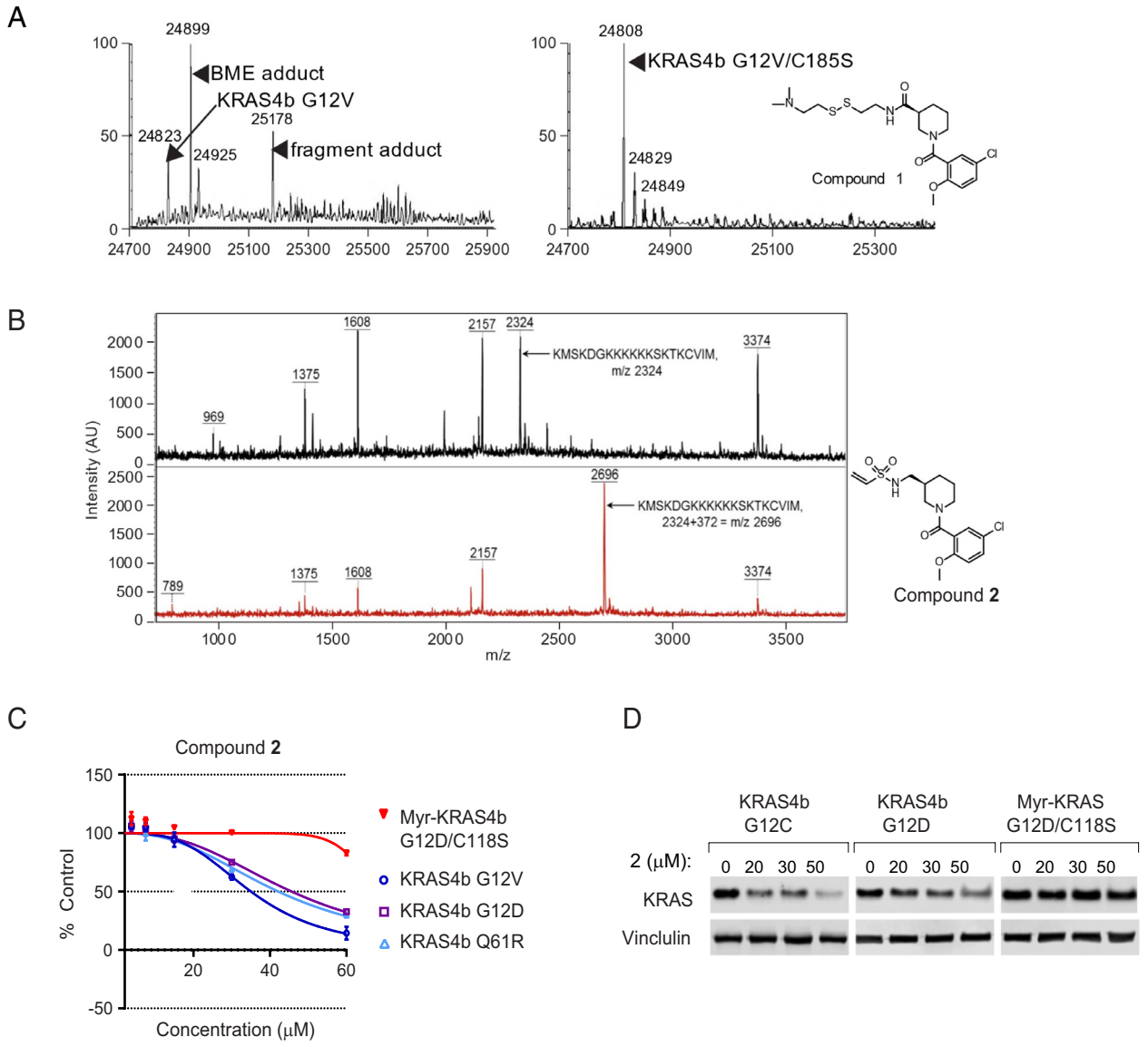

Fig. 1. Discovery and development of C185 covalent inhibitors. (*A*) Disulfide tethering hit led to discovery of compound **1**. *Left* Panel: Mass spectra of disulfide (compound **1)** tethering reaction with KRAS4b 1–188 protein. Unmodified FLAG KRAS 4b G12V is represented as 24,823 Da peak. Peak labeled as fragment adduct is FLAG KRAS4b G12V protein bearing mass addition of 355 Da corresponding to the tethered fragment. *Right* panel: disulfide hit **1** did not react with KRAS protein when C185 was mutated to serine (C185S). (*B*) MALDI-TOF MS spectra obtained after Glu-C digest of KRAS4b (1–188). *Top* panel: control protein, bottom panel: protein modified with compound **2** that is the covalent, vinyl sulfonamide analogue of tethering hit **1**. Peak m/z 2696 indicates the 372 Da mass addition to C-terminal C185. The C185 modification was the only one detected on the protein, other cysteine residues were not affected. (*C*) Covalent inhibitor **2** decreased proliferation and KRAS protein level in KRAS-dependent MEF cells. Compound **2** reduced proliferation of MEF cells driven by mutant KRAS4b, while MEFs rescued by myristoylated KRAS4b G12D/C185S were much less affected (72-h treatment). (*D*) Treatment with compound **2** decreased KRAS4b protein level in KRAS mutant MEF cells, but not in cells driven by myristoylated KRAS G12D/C185S. Compound **2** reduced levels of KRAS4b G12C and KRAS4b G12D, but not Myr-KRAS G12D/C185S. 72 h treatment with concentrations indicated on the image; Vinculin was used as a loading control.

partial proteolytic digestion and analysis of the fragments by TDP (referred to as "middle–down" MS) confirmed that C185 and only C185 of KRAS4b had been modified by compound **3** (Fig. 2*F*). These data demonstrate that the C185-targeting compound **3** blocks farnesylation and the subsequent posttranslational processing of KRAS4b in cells.

Efforts to obtain a crystal structure of the full-length (1–188) KRAS4b protein have resulted in low-resolution crystals, possibly because of the dynamic behavior of the HVR. In the absence of crystallography-based data and to better understand whether C185 in the HVR could be adjacent to a pocket in the G-domain for noncovalent binding, we performed MD simulations of full-length KRAS4b (1–188) and other major RAS isoforms. We further used SAXS and NMR spectroscopy in the absence or presence of the ligand to validate experimentally that the KRAS4b HVR can interact with the G-domain and form the pocket where our molecule binds.

MD Simulations Determine HVR Interaction with the G-Domain. We carried out a series of MD simulations of KRAS4a, KRAS4b, HRAS, and NRAS to assess whether the HVR can interact with the G-domain and whether the dynamics of all RAS proteins are similar or exhibit isoform specificity. Interestingly, the HVR of KRAS4b appears to interact with the G-domain, forming a transient tricomponent pocket comprising the HVR (aa 184–188), helix α3 (aa 90–94, 97), and helix α4 (aa 129, 132–133, 137) (Fig. 3 *A*, L*eft* Panel). Such a pocket is adjacent to (and could occasionally merge with) another transient pocket comprising the HVR (aa 184–186) and α3 (aa 97, 101), α4 (aa 137–139), and loop 7 (aa 106–108) (Fig. 3 *A*, *Right* Panel). A

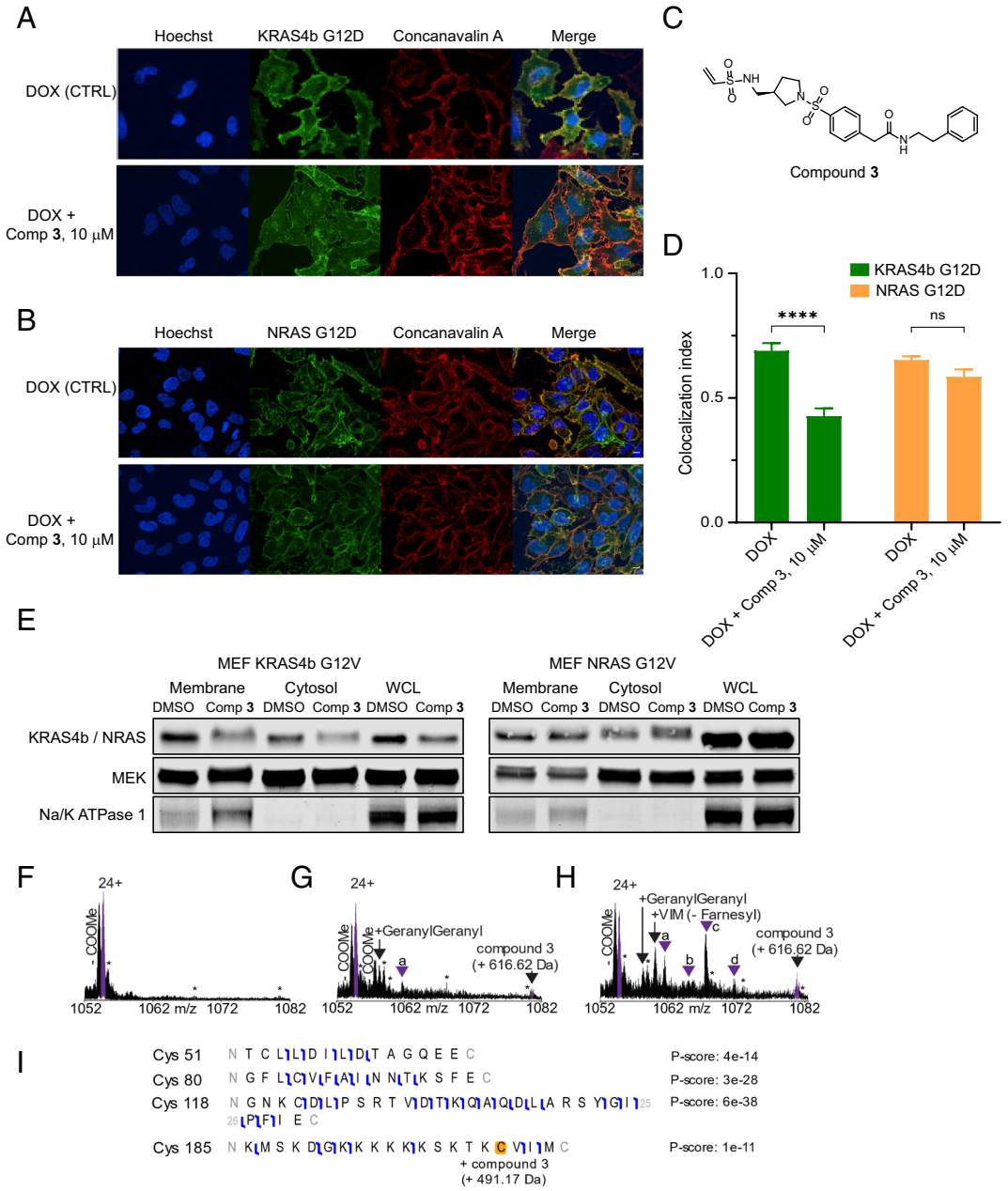

Fig. 2. Effects of compound **3** on KRAS4b but not NRAS, and C185 target engagement in cells. *(A–C)* GFP-KRAS4b G12D and GFP-NRAS G12D localization in HeLa cells. GFP-KRAS4b G12D and GFP-NRAS G12D localization was monitored in doxycycline-inducible HeLa cell lines by colocalization with concanavalin A at the plasma membrane. HeLa clonal cell lines expressing GFP-KRAS4b G12D (*A*), or GFP-NRAS G12D (*B*) were incubated with DMSO or 10 μM Compound **3** (Fig. 2*C*) for 24 h. KRAS4b G12D-expressing cells show a decrease in KRAS4b G12D localization at the membrane compared to the DMSO control. Cell nuclei were stained with Hoechst (blue) and plasma membranes were stained with Concanavalin A (red). (Scale bar, 5 μm.) (*D*) A significant difference in membrane localization of KRAS4b was observed using Pearson coefficient (mean ± SE, n = 25 for each condition). ****$P < 0.0001$ (*E*) Compound **3** decreased the amount of KRAS in MEF cells driven by KRAS4b G12V, but not in MEF cells driven by NRAS G12V. Treatment with 20 μM compound **3** for 48 h decreased KRAS4b levels in KRAS G12V MEFs. WCL – whole cell lysate. (*F–I*) Visualization of the compound **3**-bound KRAS4b proteoform by high-resolution top–down MS, employing a selected ion monitoring (SIM) method targeting the 24+ charge state of the intact protein. (*F*) KRAS4b proteoforms isolated from DMSO-treated cells; (*G*) KRAS4b proteoforms isolated from compound **3**-treated cells; (*H*) KRAS4b proteoforms isolated from cells treated with compound **3**, and a dual farnesyl- and geranylgeranyl-transferase inhibitor, L-778,123. The unprocessed KRAS4b proteoform bearing the + 491.17 Da mass shift of bound compound **3** is indicated in purple, along with the processed and farnesylated, or canonical, KRAS4b G12D proteoform (PFR 249921). Loss of C-terminal carboxymethylation (PFR 249922) is indicated by the label "-COOMe", while asterisks indicate oxidation products of electrospray ionization or other unrelated species. Inverted purple triangles indicate KRAS4b proteoforms believed to bear intermediates or metabolic products of compound **3**, with calculated mass shifts as follows: a, + 156.98 Da; b, + 221.96 Da; c, + 300.96 Da; d, + 397.99 Da from the mass of the canonical proteoform. (*I*) Localization of KRAS-bound compound **3** to the targeted Cys residue by partial proteolytic digest and subsequent middle–down MS. Example identified peptides are shown, demonstrating that the +491.17 Da mass shift of compound **3** could be localized only to Cys 185, and not to any other Cys residue within the KRAS4b sequence.

similar HVR-α3-α4 interaction outcome was observed in 21 of 26 KRAS4b simulations (accounting for ~24.4% of a total of ~35 μs simulation time), irrespective of using different HVR topology (ordered or disordered), nucleotide loading (GTP or GDP), and/or the different force fields (CHARMM or AMBER) (see *SI Appendix* for details).

From the free energy profile of the HVR binding to α3 and α4, we observed a nearly barrierless transition for the HVR to form

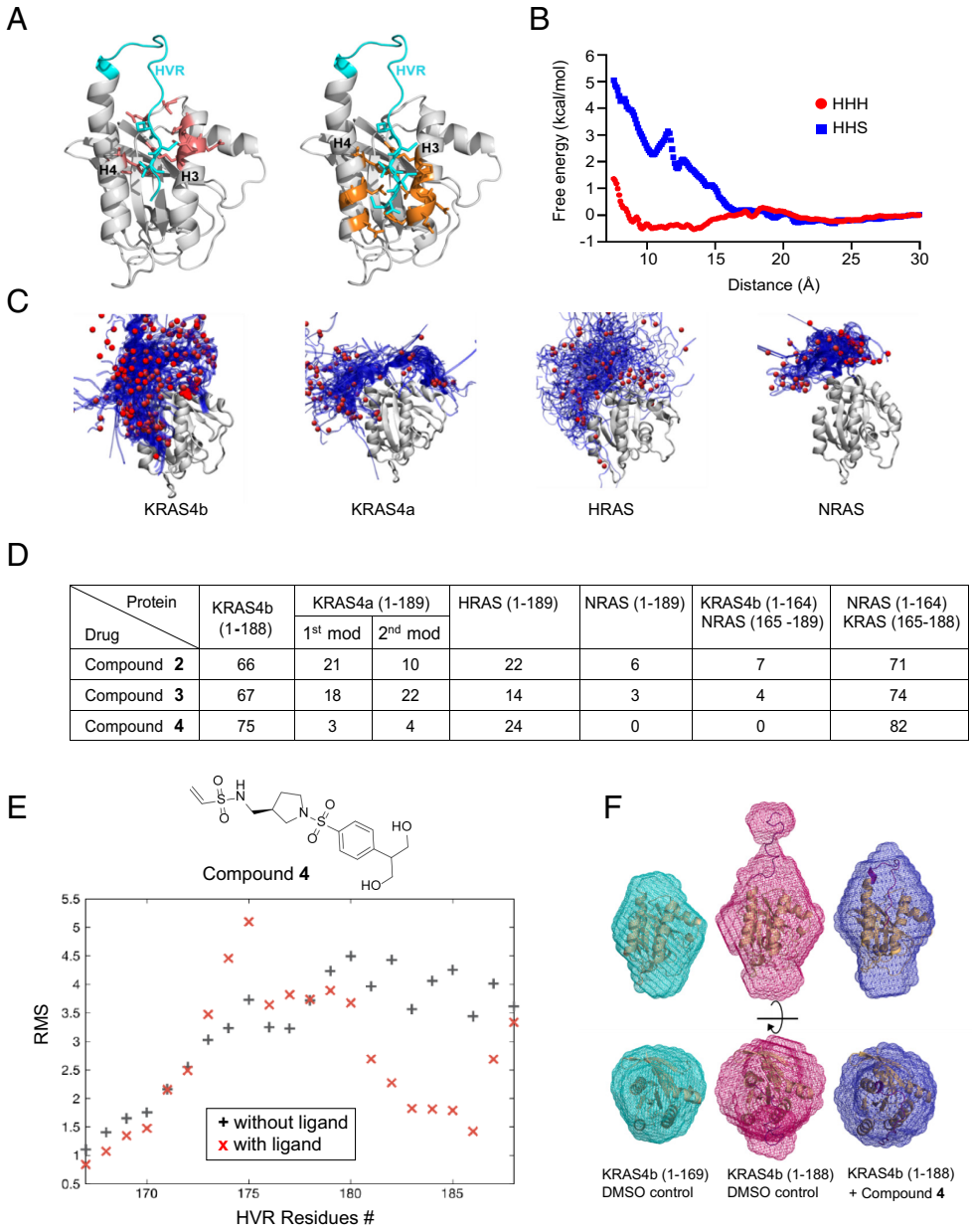

Protein / Drug	KRAS4b (1-188)	KRAS4a (1-189)		HRAS (1-189)	NRAS (1-189)	KRAS4b (1-164) NRAS (165 -189)	NRAS (1-164) KRAS (165-188)
		1st mod	2nd mod				
Compound **2**	66	21	10	22	6	7	71
Compound **3**	67	18	22	14	3	4	74
Compound **4**	75	3	4	24	0	0	82

Fig. 3. MD simulation and SAXS data identify KRAS4b HVR interactions with the G-domain. (*A*) The site maps of a tricomponent pocket formed by HVR interacting with helix3 (α3) and helix4 (α4) in the G-domain of KRAS4b. (*B*) Interactions of KRAS4b HVR with the α3/α4 site (HHH, red line) is energetically favorable over interaction of KRAS4b HVR with α3/Switch2 site (HHS, blue line). (*C*) Among four major RAS isoforms, KRAS4b exhibits unique behavior of HVR interacting with the G-domain, that is not seen for other major RAS proteins. HVR of KRAS4b only interacts with the G-domain of the protein in the region between α3/α4. (*D*) MALDI-TOF MS analysis of covalent labeling to HVR cysteine residues in RAS proteins with selected compounds. KRAS4b (1–188) shows highest degree of covalent modification to C185, and NRAS (1–189) shows the lowest. Interestingly, the high level of labeling to C185 in KRAS4b-G-domain/NRAS-HVR chimera suggests KRAS4b HVR dictates interaction with the G-domain. (*E*) Structure of compound **4** and RMSF comparison of KRAS4b HVR without ligand (black), and with compound **4** covalently attached to C185 (red). Presence of the ligand stabilizes the HVR interaction with the G-domain, especially residues 182–187. (*F*) Three-dimensional molecular envelopes reconstructed from SAXS data. Thirty-two independent DAMMIN reconstructions were run using GNOM output from three KRAS constructs: KRAS4b-1–169 (green), the full-length protein KRAS4b(1–188) (rose), and KRAS4b(1–188) with C185 covalently modified with compound **4** (purple). The dummy atom models were then aligned, averaged, and filtered using DAMAVER. The corresponding crystallographic structures fitted to the ab initio envelopes are shown in two orientations.

an energetically stable but kinetically transient conformation (tricomponent pocket; ~0.6 ± 0.1 kcal/mol), as shown by HHH, red trace in Fig. 3*B*. In contrast, transitions of the HVR binding to other areas of the G domain, for example the α3/switch-II pocket (HHS, blue trace), encounter higher energetic barriers, and therefore are less likely to form stable conformations (Fig. 3*B*).

For NRAS, the HVR is not localized to the α3 and α4 (0% of ~11 μs) or any part of the G-domain, but instead moves randomly with no specificity (Fig. 3*C*). Conversely, the HVR of KRAS4a and HRAS show some similar behavior to KRAS4b, though the frequency of HVR interactions with α3/α4 of the G-domain in KRAS4a and HRAS is significantly lower (~3.1% of ~11 μs and ~3.9% of ~11 μs, respectively; *SI Appendix*, Fig. S2). Closer examination of these μs timescale simulations and analysis of published structural data (PDB ID 2MSD) reveal that KRAS4b uses the polylysine stretch of residues (aa K175–K180) to interact with E107 and D108 in the G-domain, forming salt bridges (20). This lysine chain in KRAS4b functions as a secondary anchor required for the association of the protein with the plasma membrane (21). These salt bridge interactions may uniquely stabilize the KRAS4b

HVR to associate with the G-domain, while the other RAS isoforms lack a similar lysine-rich motif in the HVR (*SI Appendix*, Fig. S3).

The frequency of HVR interactions with the G-domain α3/α4 region across RAS isoforms mirrored their levels of covalent labeling at HVR cysteine residues. As shown in Fig. 3*D*, KRAS4b shows the highest levels of covalent labeling at C185, while NRAS shows the lowest.

Compound **4** was designed to probe the putative binding site within α3 and α4 of KRAS4b as shown in Fig. 3*A*. As designed, compound **4** shows a good level of covalent modification of C185, as informed by MALDI-TOF MS (Fig. 3*D*). MD simulation results show that compound **4** stabilizes the HVR tail (aa 181–187) into the G-domain of KRAS4b, increasing the residence time in this pocket (Fig. 3*E*).

SAXS Measurements Elucidate Alterations in KRAS4b Protein Envelope Shape When Compound Is Tethered to C185. MD simulation findings inspired us to investigate the KRAS4b conformation in solution in the absence or presence of compound **4** using SAXS. This technology has emerged as an efficient method to evaluate low-affinity protein–ligand complex structure in solution (22). We collected synchrotron radiation SAXS data for the G-domain of KRAS4b (1–169), full-length KRAS4b (1–188), and the full-length protein covalently modified with compound **4**. These data confirm the computational predictions that the presence of ligand stabilizes interactions between the HVR and G-domain of KRAS4b, shown in Fig. 3*D*. Illustrated in Fig. 3*E* are the molecular envelopes of the G-domain of KRAS (1–169) compared to the full-length KRAS4b. There is a striking difference in the molecular envelope shapes of these proteins, with the full-length protein exhibiting an extended top portion, most probably corresponding to the dynamic HVR movements. This top extension diminishes in the same construct, KRAS4b (1–188), that has been covalently modified with compound **4** (Fig. 3*F*). The electron pair-distance distribution, $P(r)$, determined from the scattering data suggests a less elongated envelope with a smaller *Dmax* in the presence of the compound (see *SI Appendix* for details*)*. This observation supports our computational predictions of a C185 inhibitor binding to a tricomponent pocket, comprising the HVR-α3-α4 of KRAS4b, and sequestering the HVR proximal to the G-domain.

Heteronuclear NMR Identifies the Binding Site of Compound 4. Comparison of NMR assignments of KRAS4b (1–188)-GDP (assigned 2D ^{1}H-^{15}N HSQC spectrum of KRAS4b (1–188), *SI Appendix*, Fig. S4*A*, BMRB ID: 50623) and KRAS4b (1–169)-GDP facilitated the identification of G-domain residues that exhibited significant structural differences due to interactions with the HVR. Chemical shift differences depicted in Fig. 4*A* identify such significant residues within the β1-β3 region (aa 3,5,6, 44,45, 47–51), the loop between α3 and β5 (aa 106–109, 111,112), and helix α5 (aa 157, 159–169) (*SI Appendix*, Fig. S4 *B* and *C*) (23).

To understand the compound binding site, we determined the solution structures of KRAS4b (1–188)-GDP of the DMSO-d_6 treated sample. A structural ensemble is shown in Fig. 4*B* (RCSB ID: 7KYZ) (also *see SI Appendix*, Fig. S4 *D* and *E* and Table S1). The converged structural fold is composed of 5 α-helices (aa 16-25, 66-74, 87-104, 127-137, 151-173) and 6 β-strands (aa 2–8, 40–46, 49–57, 77–83, 111–116, 141–143). Residues 176–188 of the HVR show conformational dynamics. The range of these secondary structural elements compares well with those in the reported crystal structures (RCSB ID 5TAR and 6MBT) (24, 25). In agreement with the chemical shift perturbation (CSP) NMR and MD simulation data, analysis of our structural ensemble (RCSB ID: 7KYZ) identifies a dominant cluster of six structures (out of 20 reported) in which the HVR adopts a conformation that is closer to the α3-α4helical plane. There is a 30% likelihood of preferential packing near this region. In the remaining structures, HVR conformations exhibit a more randomized order (see *SI Appendix* for details*)*.

Covalent modification of C185 by compound **4** resulted in significant residue perturbation in the G-domain as well as in the HVR as demonstrated by the 2D ^{1}H-^{15}N HSQC overlay (*SI Appendix*, Fig. S4*F*). Interestingly, G-domain residues K88, E91, H94, R97, and E98 (α3), D108 (loop connecting α3 and β5), I163, K165-K167 (α5), and HVR residues T183-C185, I187, and M188 elicited significant CSPs and apparently play an important role in defining the binding pocket.

Atomistic evidence of HVR binding to the G-domain came from 3D NOESY spectral analysis of compound **4**-tethered KRAS4b (1-188) that yielded a total of nine unambiguous NOEs between the select residues in the HVR and the G-domain. These HVR-G-domain residue pairs are M188(HVR)-F82(β4), I187(HVR)-E91(α3), and I187(HVR)-D92(α3) (Fig. 4*C* and *SI Appendix*, Fig. S4 *G* and *H*). Observation of such NOEs is likely attributed to the inherent noncovalent affinity of compound **4** that guides the HVR in transitioning to a conformationally more constrained environment. Next, we combined distance restraints deduced from these NOEs with the structural restraints of KRAS4b (in the absence of compound) and calculated the structural model of KRAS4b-compound **4** complex in a CSP-analysis-guided manner. Notably, the calculated structure ensemble shows the HVR typically converged upon and stabilized within the α3-α4 region (Fig. 4*D* and *SI Appendix*, Fig. S4*I* and Table S2), thus defining the compound **4** binding site. Apparently, these NOEs were sufficient in elucidating the binding character of compound **4** that mediates HVR occupancy to the HVR-α3-α4 pocket. Overall, the structural fold of intermolecular protein–ligand complex corroborates the energetically favored structural conformers identified in the MD simulation data, and validates the molecular shape determined based on the SAXS data.

Discussion

With *KRAS* being the most frequently mutated oncogene in each of the three deadliest cancers in the United States (lung, colorectal, and pancreatic cancer), the development of anti-KRAS therapies is a major priority and challenge for cancer research. RAS proteins did not appear to present suitable pockets to which drugs could bind, except for the GDP/GTP binding site. Unfortunately, RAS proteins bind these nucleotides with very high (picomolar) affinities, making the development of effective nucleotide analogs virtually impossible.

Recently, the covalent KRAS G12C inhibitors sotorasib (AMG510) and adagrasib (MRTX849) have been approved for treatment of cancers expressing this allele (26, 27). Compounds that target the KRAS G12D allele, such as MRTX1133, are also in clinical trials.

Pan-KRAS inhibitors that block signaling from the major oncogenic alleles, including the most prevalent G12D and G12V mutations, would benefit a large population of patients affected by KRAS-driven cancers. Pan-KRAS inhibitors would provide additional advantage of targeting tumors that have acquired resistance to KRAS G12C inhibitors. Accordingly, there remains a need for both allele-specific and pan-KRAS inhibitors, and the latter could be used to treat KRAS-driven cancers regardless of their mutation status.

In strong support of pan-KRAS inhibitor development, Barbacid's laboratory has recently shown that total ablation of the

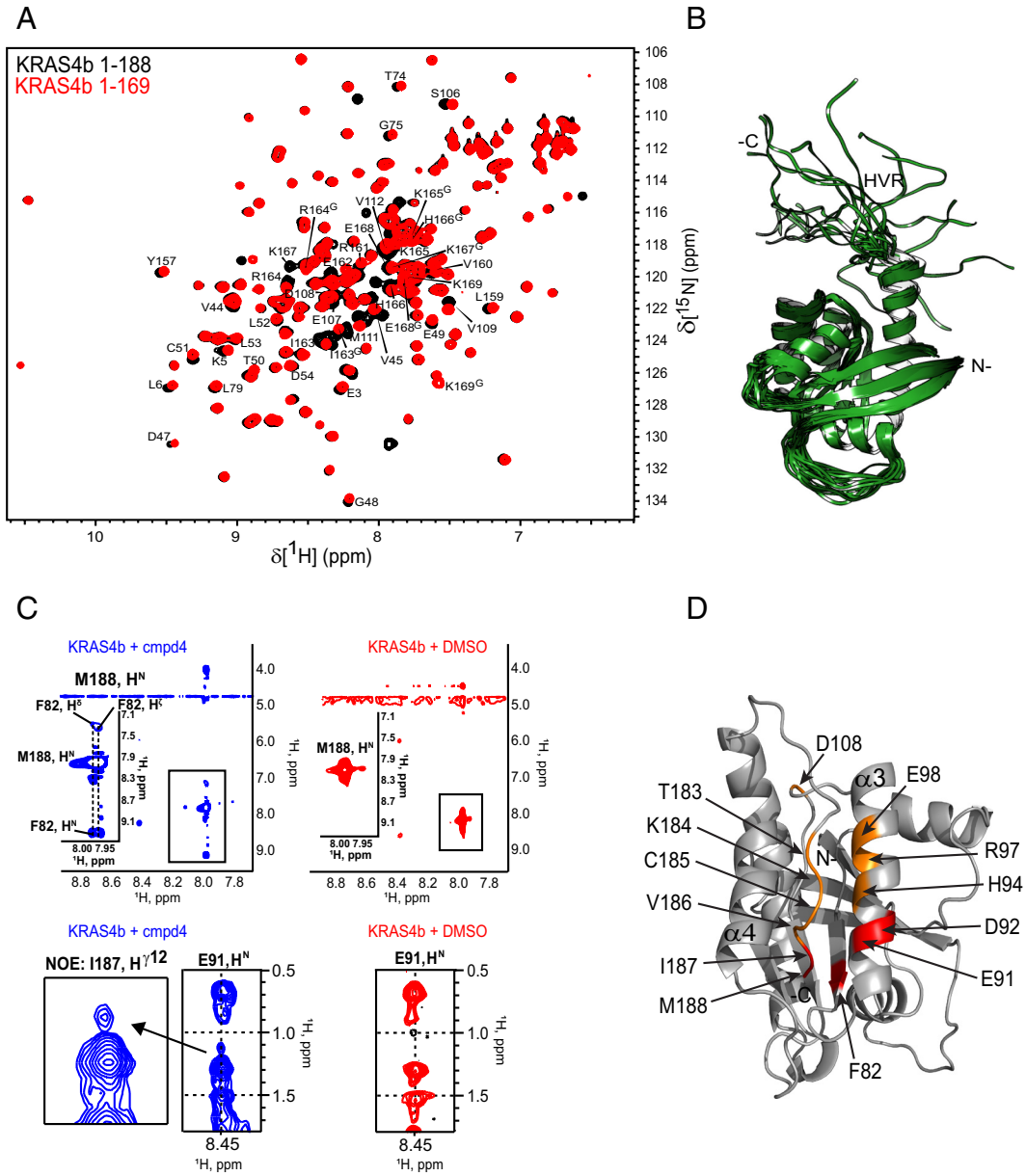

Fig. 4. Heteronuclear NMR for binding site identification of compound **4**. (*A*) 2D ^{1}H-^{15}N HSQC spectra comparison of the G-domain of KRAS4b (1–169) and the full-length protein (1–188) indicates differences in chemical shifts resulting from the interaction of the HVR with the G-domain. Residues eliciting effective CSP (*SI Appendix*, Fig. S4 *B* and *C*) are highlighted by single-letter amino acid sequence followed by its sequence number. CSP residue names superscripted with letter "G" belong to the G-domain. Unassigned crosspeaks in black do not belong to the G-domain residues. (*B*) Ensemble of 20 solution structures of KRAS4b (1–188). AA residues 174–188 of HVR at C-terminus are found conformationally flexible. (*C*) Detection of intramolecular NOE contacts between the aa residues in the HVR and the catalytic G-domain in KRAS4b (1–188) with compound **4** covalently attached to C185, as determined in the ^{15}N-edited-NOESY-HSQC and ^{13}C-edited NOESY-HSQC spectra at 25 °C (See *SI Appendix*, Fig. S4 *G* and *H* for additional such NOEs detected between the HVR and the G-domain). *Top* panels: amide protons (H^N) of M188 and its conformer show NOE with amide proton (H^N) of residue F82 and with aromatic ring protons (H^{δ} and H^{ε}) rendered blue. *Bottom* panels, amide proton (H^N) of E91 shows NOE with side-chain methylene proton ($H\gamma^{12}$) of residue I187. Magnified view on left represents spectral regions in black boxes. None of the NOEs overlap with proton chemical shifts of compound **4**. No such NOEs were observed in the samples treated with DMSO (in absence of compound **4**), as seen in panels shown in red. (*D*) Representative solution structure of KRAS4b (1–188) upon inclusion of 7 intramolecular NOEs that are observed between the HVR residues I187 and M188, and G-domain residues F82, E91, and D92; these residues are shown in red. Rendered orange are the residues that show significant CSP (deduced from HSQC overlay of KRAS4b (1–188) treated with DMSO vs tethered with compound **4**) in the tricomponent binding region (HVR-α3-α4).

KRAS gene is well tolerated in adult mice, and causes a complete regression of KRAS-driven tumors (28). On the other hand, ablation of all three RAS genes was fatal in mice. These data underscore the importance of KRAS selectivity over HRAS and NRAS in the development of pan-KRAS inhibitors. Potential pan-KRAS drugs that bind to the G-domain are undergoing clinical and preclinical evaluation. Compounds that covalently block C185 in KRAS4b, preventing its posttranslational modification and subsequent membrane attachment, represent an alternative approach to the development of a pan-KRAS inhibitor.

Our efforts to covalently target C185 in KRAS4b have revealed a pocket formed by the HVR and α3-α4. This pocket localizes between α3 and α4 and has not been recognized before as a potential site where small molecules can bind. However, KRAS4b HVR plays a role in forming this pocket that could not be present in the fully processed KRAS4b when HVR is posttranslationally modified, nor KRAS4a, NRAS, and HRAS. Based on our MD simulations, the HVRs of HRAS and KRAS4a interact with the α3/α4 region of the G-domain for only a small fraction of the simulation time and exhibit a random sampling behavior, whereas

the HVR of NRAS does not interact with the α3/α4 region at all. In a study reported by Mazhab-Jafari et al., one of the structural models showed direct interactions between residue K177 (HVR) and residues E107/D108 (G-domain) (20). According to these data, the polylysine stretch of the HVR could play a role in HVR localization to the G-domain by forming salt bridge interactions in KRAS4b; such an interaction was observed in our MD simulations as well. Our CSP measurements are congruent with the G-domain/full-length 2D ^{1}H-^{15}N HSQC comparison data that indicate E107/D108 as potential perturbing residues, possibly due to the HVR interaction. Residues E107 and D108 are conserved among all major RAS isoforms; however, the presence of the polylysine stretch in the HVR is unique to KRAS4b (KRAS4a HVR has a single lysine residue (K175), while NRAS and HRAS have none).

It has been shown that the engineered RAS binding effectors K13 and K19 Darpins bind to the α3-loop7-α4 region of KRAS and inhibit protein function (29) by not only preventing RAS dimerization and clustering, but also by impacting nucleotide exchange (29, 30). Our presented small molecules modify C185 and bind to the HVR-α3-α4 pocket in an E107/D108 (loop7)-binding-assisted manner.

In conclusion, we identified compounds that covalently react with C185 and demonstrate a unique mechanism of KRAS inhibition. The compounds exploit a previously unobserved pocket formed by the interaction of the KRAS4b HVR with the G-domain, thus preventing prenylation and inhibiting this predominant splice variant's activity. These compounds inhibit the proliferation of KRAS4b-dependent MEFs and are significantly less active against MEFs whose proliferation is driven by myristoylated KRAS4b lacking the prenylation site at C185. This study represents a starting point for the development of more active and potent KRAS4b-specific inhibitors. KRAS4a has been shown dispensable for mouse development and homeostasis. The absence of KRAS4b cannot be compensated for by its splice variant KRAS4a due to the lower levels of expression of KRAS4a in most tissues (31, 32). However, despite these lower levels of expression, mutant KRAS4a was able to induce lung adenocarcinoma in mice in the absence of the KRAS4b isoform (32). More data are needed to understand whether eliminating the KRAS4b isoform alone would have a therapeutic benefit, or if KRAS4a will compensate as an oncogenic driver.

Materials and Methods

Chemical Synthesis, QC Validation, and NMR of Small Molecule Targets. Detailed synthesis is provided in SI. LC–MS and ^{1}H-NMR analysis was performed upon all intermediates and target molecules for structural determination. Compounds submitted for biological evaluation were deemed to be > 95% purity and were stored at −20 °C to prevent decomposition. LC–MS analysis was performed using an Agilent 6,120b single quadrupole mass spectrometer with an Agilent 1,260 infinity II chromatography separations module and Agilent 1,260 infinity II photodiode array detector controlled by Agilent Chemstation software. The HPLC column used was an Agilent ZORBAX Eclipse XDB-C18 4.6 × 150, 3.5u Rapid Resol column with a mobile phase of water (0.1 % formic acid)/MeCN (0.1% formic acid) and a gradient of 5 to 95% MeCN over 10 min at a flow rate of 1 mL/min. Accurate mass data were obtained using a Thermo Fisher Exactive plus EMR orbitrap LC–MS system. Exact mass values were calculated by ChemCalc. ^{1}H-NMR spectra were obtained from samples dissolved in an appropriate deuterated solvent ($CDCl_3$, D_2O, DMSO-d_6, Acetone-d_6) using a Varian Mercury 400 MHz Spectrometer. Spectral analysis was performed in MestReNova™ v11 (33).

Cloning, Expression, and Purification of Recombinant KRAS Proteins. Sequence validated gateway entry clones for KRAS4b (1–188) and KRAS4b (1–169) were generated by standard cloning methods. Recombinant constructs incorporate an upstream His_6 and maltose-binding protein (MBP), followed by tobacco etch virus (TEV) protease cleavage site (ENLYFQG), ending with the appropriate KRAS sequences, and served as final *Escherichia coli* expression clones. The BL21 STAR (*rne131*) *E. coli* strain containing the DE3 lysogen and rare tRNAs (pRare plasmid, Cm^R) was transformed with the expression plasmids (Amp^R) (34). Unlabeled and isotopically $^{13}C/^{15}N$ or ^{15}N labeled KRAS4b(1–188) and KRAS4b (1–169) samples were obtained using the methods as previously described (24). Proteins were purified using metal-affinity chromatography and subsequently NGC chromatography (BioRad, Hercules, CA). Protein samples were frozen at −80 °C until further use. See *SI Appendix* for detailed methods.

Cell Proliferation Assay. Cell viability in the presence of compounds was measured using CellTiter-Glo (Promega). Cells were plated in black-walled 384-well plates (Greiner, 781091) at densities in accordance with their doubling time (for MEFs typically 1,000 cells/well in 20 μL), using the Multidrop Combi Reagent Dispenser (Thermo). Cells were incubated overnight at 37 °C in a humidified atmosphere of 5% CO_2 prior to drug addition. Compound and DMSO addition to microplates was performed using the Access Laboratory Workstation (Labcyte) and Echo 555 (Labcyte) liquid handler. See *SI Appendix* for details. Cellular ATP levels (an indicator of cell count) were determined with CellTiter-Glo (CTG, Promega G7573) luminescence assay using an EnVision Plate Reader (PerkinElmer). Measurements of cell growth inhibition were made using cell population at the time of compound addition (T0) and at 72 h incubation time (T72) using the following equation:

$$\frac{T72 - T0}{C - T0} \times 100.$$

Dose–response curves were generated using Prism 7 software (GraphPad).

Confocal Microscopy and Colocalization analysis of RAS Localization Experiment. Doxycycline-inducible GFP-KRAS4b G12D and GFP-NRAS G12D HeLa cell clones were seeded into glass-bottomed 12-well plates at 4e5 and 8e5 cells per well, respectively, in 1 mL 10% FBS phenol-red free DMEM. Even densities were achieved after 24 h due to differential growth rates. Doxycycline was then added to wells to achieve concentrations of 400 ng/mL for NRAS G12D- and 500 ng/mL for KRAS4b G12D-expressing cells. After 4 h of incubation at 37 °C 5% CO_2, medium was replaced with fresh, complete DMEM containing doxycycline and DMSO (0.088%) or 10 μM compound **3**. After 24 h of incubation, wells were washed twice with PBS, fixed with 4% formaldehyde PBS for 20 min at room temperature, and then washed twice again with PBS. Later, cell nuclei were stained with 500 μL per well of 1 μg/mL Hoechst diluted in PBS for 15 min at room temperature. Wells were washed twice with PBS, and then cell membranes were stained using 1 mL 5 μg/mL Concanavalin A (Con A- Alexa 647) diluted in PBS at room temperature for 10 min. Wells were then washed three times with PBS to eliminate excess dye.

Using the AX-Nikon Laser Scan Confocal system, we captured z-stacks comprising seven planes of five to seven different fields of view in each condition. To image fluorescent proteins, 488 nm and 647 nm solid state lasers were used together with GFP 500/550 nm and deep red 663/738 nm emission filters.

Image analysis was performed with ImageJ/Fiji using the plugin colocalization threshold. Briefly, we selected five different regions of interest (ROIs) corresponding to single cells in the different fields of view. Each ROI was processed individually. To calculate RAS membrane localization, we obtained the correlation between KRAS4b G12D or NRAS G12D and the plasma membrane marker Concanavalin A. The corresponding values for Pearson correlation coefficients were plotted and analyzed in GraphPad Prism software.

Cell Fractionation. MEF cells were seeded into sixteen 10 cm dishes for each cell line at (5e5 cells/dish) and allowed to grow overnight. Cells were treated with either 0.1% DMSO or 20 μM compound **3**, with 8 dishes treated per condition for each cell line. Cells were drug- or DMSO-treated again, 24 h after the initial treatment. After another 24 h of incubation, whole cell lysate (WCL) samples were collected from 2 dishes for each treatment. Cells were washed with PBS and lysed using RBD buffer. Cell lysates were spun at 20,000×*g* for 15 min, the resulting supernatants transferred to new microcentrifuge tubes, and samples were frozen at −80 °C.

Cell fractionation samples were collected from 7 dishes for each treatment according to the published protocol (35). Cells were washed twice with hypotonic homogenization buffer (10 mM HEPES at pH 7.4, 10 mM KCl, and 1.5 mM $MgCl_2$),

then harvested in hypotonic homogenization buffer by scraping and collecting into tubes. Cell mixture was freeze/thawed three times. Samples were centrifuged at 500×*g* for 10 min to remove unbroken cells and nuclei, and supernatant moved to a new tube. This step was repeated three more times until no visible pellet was produced. The post nuclear supernatant was moved to an ultracentrifuge tube and spun at 300,000×*g* for 1 h at 4 °C. Supernatant was collected as the cytosolic fraction. Pellet was washed with 3 mL of cold D-PBS without disturbing it. PBS was removed by vacuum, and this step was repeated one more time. The pellet was fully resuspended in an appropriate volume of RBD buffer as the membrane fraction. Protein quantification was performed by BCA assay. Thirty two μg of protein from each fraction was loaded to the gel.

Proteomics, Liquid Chromatography, and MS. Cell Lysis was performed as follows; Frozen cell pellets (each containing approximately 2E+08 cells) were thawed on ice, followed by resuspension in ice-cold lysis buffer [50 mM Tris, pH 7.5, containing 150 mM NaCl, 0.5% NP-40 (IGEPAL CA-630, Sigma Aldrich), 0.5% BioXtra NP-40 substitute (Sigma Aldrich), and 1X final concentration of HALT Protease and Phosphatase Inhibitor Cocktail (Thermo Fisher Scientific)] at an approximate ratio of 1 mL per 3E+07 cells. Lysates were incubated for 30 min on ice, with gentle resuspension every 10 min, sonicated for 30 s (amplitude 50%, 2 s on, 5 s off, all on ice) using a Sonic Dismembrator (Fisher Scientific), and clarified by centrifugation for 30 min at 3,200×*g* and 4 °C.

Immunoprecipitation, top–down and middle–down MS and liquid chromatography of untreated- and compound-treated KRAS4b (1–188) samples were carried out using procedures detailed in *SI Appendix*.

Computational MD Simulation and SAXS Data Collection. Methods used are detailed in *SI Appendix*.

Heteronuclear NMR. $^{13}C/^{15}N$- or ^{15}N-labeled samples of GDP loaded KRAS4b (1–188) and KRAS4b (1–169) of 0.85 to 1.0 mM were used. Samples were prepared either in buffer A (20 mM HEPES pH 7.3, 150 mM NaCl, and 2 mM $MgCl_2$) or buffer B (20 mM MES pH 6.5, 150 mM NaCl, and 2 mM $MgCl_2$) for all NMR data collection. Samples contained 10% D_2O, 0.25 mM DSS as internal standard, and 0.05% (w/v) NaN_3. NMR experiments were performed at 298 K on Bruker Avance spectrometers of field strengths of 700 MHz, 800 MHz, or 900 MHz all equipped with 5-mm TCI cryoprobe. Data were collected in the gradient-selected sensitivity-enhanced mode (36, 37) (see *SI Appendix* for details). All NMR data were processed in NMRPipe/NMRDraw (38), and visualized and analyzed in CCPNMR analysis v2.4 (39). Effect of compound **4** binding on KRAS4b structural conformation was determined by using the structural NMR data of unmodified KRAS4b (treated with DMSO-d_6) and modified KRAS4b-compound **4** [compound is tethered to C185 of KRAS4b (1–188)]. ^{13}C-edited NOESY-HSQC and ^{15}N-edited NOESY-HSQC experiments were carried out for both the unmodified and compound-modified KRAs4b. Solution structures were determined in the programs Ponderosa-C/S (40), and Cyana-3.98 (41). *SI Appendix* provides additional details on data analysis for CSP, solution structure determination, and NMR-guided structures of protein–ligand complex between KRAS4b(1–188)-GDP and compound **4**.

Data, Materials, and Software Availability. The NMR chemical shift assignments and structure coordinates for the full-length KRAS4b GDP (unmodified protein) have been deposited in the BioMagResBank, https://bmrb.io/ [accession IDs 50623 (42) and 30825 (43)] and in the Protein Data Bank, https://www.rcsb.org/ (PDB ID 7KYZ) (44), respectively. All other data are included in the article and/or supporting information.

ACKNOWLEDGMENTS. We acknowledge the following personnel of Protein Expression Laboratory, Frederick National Laboratory for Cancer Research, for work performed on cloning, protein expression, and purification (listed alphabetically): John-Paul Denson, Peter Frank, Jennifer Mehalko, Shelley Perkins, Rosemilia Reyes, Mukul Sherekar, Troy Taylor, Vanessa Wall. We thank William Burgan and Katie Powell for development of MEF cell lines, and Shibani Bhattacharya and Michael Goger of New York Structural Biology Centerfor help with NMR data collection. We acknowledge use of SAXS Core Facility of Center for Cancer Research (CCR), National Cancer Institute (NCI), funded by FNLCR contract 75N91019D00024 and the intramural research program of the NIH, NCI, CCR. This research used 12-ID-B beamline of the Advanced Photon Source, a U.S. Department of Energy (DOE) Office of Science User Facility operated for the DOE Office of Science by Argonne National Laboratory under Contract No. DE-AC02-06CH11357. We thank the computing support from Lawrence Livermore National Laboratory (LLNL) Institutional Computing Grand Challenge program. The computational work was supported in part by the Joint Design of Advanced Computing Solutions for Cancer (JDACS4C) program established by the US DOE and the NCI, and was performed under the auspices of the US DOE by LLNL under Contract DE-AC52-07NA27344. Release: LLNL-JRNL-853943. Top–down and middle–down proteomic analyses were performed at the National Resource for Translational and Developmental Proteomics at Northwestern University, funded by NIH Grant P41 GM108569. We thank Ryan T. Fellers, Joseph B. Greer, and Bryan P. Early for assistance with middle–down data analysis and compound localization. This project was developed and funded through the collaboration with BridgeBio Inc. under cCRADA, and in part with federal funds from NCI, NIH Contract 75N91019D00024.

Author affiliations: [a]National Cancer Institute RAS Initiative, Cancer Research Technology Program, Frederick National Laboratory for Cancer Research, Frederick, MD 21701; [b]Lawrence Livermore National Laboratory, Physical and Life Sciences Directorate, Biotechnology and Biosciences Division, Livermore, CA 94550; [c]Department of Biochemistry and Molecular Genetics, College of Medicine, University of Illinois at Chicago, Chicago, IL 60607; [d]Basic Science Program, Frederick National Laboratory for Cancer Research, Small-Angle X-ray Scattering Facility of the National Cancer Institute, Frederick, MD 21702; [e]Department of Molecular Biosciences, Northwestern University, Evanston, IL 60208; [f]Department of Chemistry, Proteomics Center of Excellence, Northwestern University, Evanston, IL 60208; [g]Department of Cellular and Molecular Pharmacology, Helen Diller Family Comprehensive Cancer Center, University of California, San Francisco, CA 94158; [h]Department of Pharmaceutical Chemistry, Small Molecule Discovery Center, University of California, San Francisco, CA 94143; and [i]Departments of Chemical and Biological Engineering, Chemistry, and Molecular Biosciences, the Chemistry of Life Processes Institute, and the Proteomics Center of Excellence, Northwestern University, Evanston, IL 60208

Author contributions: A.E.M., Y.Y., A.K.S., V.G., F.C.L., D.V.N., and F.M. designed research; A.E.M., Y.Y., A.K.S., D.M.T., C.J.D., H.A., L.F., B.P.S., V.K., M.D., M.R., J.A.C.B., A.B., T.T., S.F., C.A., A.L.W., S.G., A.H.C., D.K.S., and O.C. performed research; L.A., L.F., W.G., S.M., D.E., A.G.S., M.A., A.R., and N.L.K. contributed new reagents/analytic tools; A.E.M., Y.Y., A.K.S., D.M.T., C.J.D., H.A., L.F., B.P.S., V.K., M.D., J.A.C.B., C.A., A.C., D.S., O.C., V.G., and F.C.L. analyzed data; A.K.S., D.M.T., C.J.D., B.P.S., M.D., and O.C. prepared samples; M.R. contributed WB Data; and A.E.M., Y.Y., A.K.S., D.V.N., and F.M. wrote the paper.

1. J. L. Bos, ras oncogenes in human cancer: A review. *Cancer Res.* **49**, 4682–4689 (1989).
2. J. Downward, Targeting RAS signalling pathways in cancer therapy. *Nat. Rev. Cancer* **3**, 11–22 (2003).
3. I. A. Prior, P. D. Lewis, C. Mattos, A comprehensive survey of Ras mutations in cancer. *Cancer Res.* **72**, 2457–2467 (2012).
4. G. W. Reuther, C. J. Der, The Ras branch of small GTPases: Ras family members don't fall far from the tree. *Curr. Opin. Cell Biol.* **12**, 157–165 (2000).
5. D. K. Simanshu, D. V. Nissley, F. McCormick, RAS proteins and their regulators in human disease. *Cell* **170**, 17–33 (2017).
6. S. Eisenberg, Y. I. Henis, Interactions of Ras proteins with the plasma membrane and their roles in signaling. *Cell Signal* **20**, 31–39 (2008).
7. P. A. Konstantinopoulos, M. V. Karamouzis, A. G. Papavassiliou, Post-translational modifications and regulation of the RAS superfamily of GTPases as anticancer targets. *Nat. Rev. Drug Discov.* **6**, 541–555 (2007).
8. V. L. Boyartchuk, M. N. Ashby, J. Rine, Modulation of Ras and a-factor function by carboxyl-terminal proteolysis. *Science* **275**, 1796–1800 (1997).
9. J. F. Hancock, K. Cadwallader, H. Paterson, C. J. Marshall, A CAAX or a CAAL motif and a second signal are sufficient for plasma membrane targeting of ras proteins. *EMBO J.* **10**, 4033–4039 (1991).
10. I. Ahearn, M. Zhou, M. R. Philips, Posttranslational modifications of RAS proteins. *Cold Spring Harb Perspect. Med.* **8**, a031484 (2018).
11. N. E. Kohl *et al.*, Inhibition of farnesyltransferase induces regression of mammary and salivary carcinomas in ras transgenic mice. *Nat. Med.* **1**, 792–797 (1995).
12. D. B. Whyte *et al.*, K- and N-Ras are geranylgeranylated in cells treated with farnesyl protein transferase inhibitors. *J. Biol. Chem.* **272**, 14459–14464 (1997).
13. C. I. Nnadi *et al.*, Novel K-Ras G12C Switch-II covalent binders destabilize RAS and accelerate nucleotide exchange. *J. Chem. Inf. Model* **58**, 464–471 (2018).
14. D. A. Erlanson, R. S. McDowell, T. O'Brien, Fragment-based drug discovery. *J. Med. Chem.* **47**, 3463–3482 (2004).
15. W. K. Gillette *et al.*, Farnesylated and methylated KRAS4b: High yield production of protein suitable for biophysical studies of prenylated protein-lipid interactions. *Sci. Rep.* **5**, 15916 (2015).
16. D. Esposito, A. G. Stephen, T. J. Turbyville, M. Holderfield, New weapons to penetrate the armor: Novel reagents and assays developed at the NCI RAS Initiative to enable discovery of RAS therapeutics. *Semin Cancer Biol.* **54**, 174–182 (2019).
17. T. K. Toby *et al.*, A comprehensive pipeline for translational top-down proteomics from a single blood draw. *Nat. Protoc.* **14**, 119–152 (2019).
18. L. Gutierrez, A. I. Magee, C. J. Marshall, J. F. Hancock, Post-translational processing of p21ras is two-step and involves carboxyl-methylation and carboxy-terminal proteolysis. *EMBO J.* **8**, 1093–1098 (1989).

19. Q. Dai *et al.*, Mammalian prenylcysteine carboxyl methyltransferase is in the endoplasmic reticulum. *J. Biol. Chem.* **273**, 15030–15034 (1998).
20. M. T. Mazhab-Jafari *et al.*, Oncogenic and RASopathy-associated K-RAS mutations relieve membrane-dependent occlusion of the effector-binding site. *Proc. Natl. Acad. Sci. U.S.A.* **112**, 6625–6630 (2015).
21. J. F. Hancock, H. Paterson, C. J. Marshall, A polybasic domain or palmitoylation is required in addition to the CAAX motif to localize p21ras to the plasma membrane. *Cell* **63**, 133–139 (1990).
22. D. I. Svergun, Small-angle X-ray and neutron scattering as a tool for structural systems biology. *Biol. Chem.* **391**, 737–743 (2010).
23. T. S. Chavan *et al.*, High-affinity interaction of the K-Ras4B hypervariable region with the Ras active site. *Biophys. J.* **109**, 2602–2613 (2015).
24. S. Dharmaiah *et al.*, Structural basis of recognition of farnesylated and methylated KRAS4b by PDEdelta. *Proc. Natl. Acad. Sci. U.S.A.* **113**, E6766–E6775 (2016).
25. S. Dharmaiah *et al.*, Structures of N-terminally processed KRAS provide insight into the role of N-acetylation. *Sci. Rep.* **9**, 10512 (2019).
26. F. Skoulidis *et al.*, Sotorasib for lung cancers with KRAS p. G12C mutation. *N. Engl. J. Med.* **384**, 2371–2381 (2021).
27. P. A. Janne *et al.*, Adagrasib in non-small-cell lung cancer harboring a KRAS(G12C) mutation. *N. Engl. J. Med.* **387**, 120–131 (2022).
28. M. Salmon *et al.*, Kras oncogene ablation prevents resistance in advanced lung adenocarcinomas. *J. Clin. Invest.* **133**, e164413 (2023).
29. N. Bery *et al.*, KRAS-specific inhibition using a DARPin binding to a site in the allosteric lobe. *Nat. Commun.* **10**, 2607 (2019).
30. D. K. Simanshu, M. R. Philips, J. F. Hancock, Consensus on the RAS dimerization hypothesis: Strong evidence for lipid-mediated clustering but not for G-domain-mediated interactions. *Mol. Cell* **83**, 1210–1215 (2023).
31. S. J. Plowman *et al.*, While K-ras is essential for mouse development, expression of the K-ras 4A splice variant is dispensable. *Mol. Cell Biol.* **23**, 9245–9250 (2003).
32. M. Salmon *et al.*, KRAS4A induces metastatic lung adenocarcinomas in vivo in the absence of the KRAS4B isoform. *Proc. Natl. Acad. Sci. U.S.A.* **118**, e2023112118 (2021).
33. M. R. Willcott, MestRe nova. *J. Am. Chem. Soc.* **131**, 13180 (2009).
34. T. Taylor, J. P. Denson, D. Esposito, Optimizing expression and solubility of proteins in *E. coli* using modified media and induction parameters. *Methods Mol. Biol.*
35. M. Zhou, M. R. Philips, Nitrogen cavitation and differential centrifugation allows for monitoring the distribution of peripheral membrane proteins in cultured cells. *J. Vis. Exp.* **126**, 56037 (2017).
36. T. J. Norwood, J. Boyd, I. D. Campbell, Improved resolution in 1H-detected 1H–15N correlation experiments. *FEBS Lett.* **255**, 369–371 (1989).
37. M. Sattler, J. Schleucher, C. Griesinger, Heteronuclear multidimensional NMR methods for the structure determination of proteins in solution employing pulsed field gradients. *Prog. NMR Spectrosc.* **34**, 93–158 (1999).
38. F. Delaglio *et al.*, NMRPipe: A multidimensional spectral processing system based on UNIX pipes. *J. Biomol. NMR* **6**, 277–293 (1995).
39. W. F. Vranken *et al.*, The CCPN data model for NMR spectroscopy: Development of a software pipeline. *Proteins* **59**, 687–696 (2005).
40. W. Lee, C. M. Petit, G. Cornilescu, J. L. Stark, J. L. Markley, The AUDANA algorithm for automated protein 3D structure determination from NMR NOE data. *J. Biomol. NMR* **65**, 51–57 (2016).
41. P. Guntert, C. Mumenthaler, K. Wuthrich, Torsion angle dynamics for NMR structure calculation with the new program DYANA. *J. Mol. Biol.* **273**, 283–298 (1997).
42. A. K. Sharma, A. E. Maciag, NMR 1H, 13C, 15N resonance assignment of the full-length K-Ras bound to GDP. BioMagResBank. https://bmrb.io/data_library/summary/index.php?bmrbId=50623. Deposited 9 December 2020.
43. A. K. Sharma, A. E. Maciag, NMR 1H, 13C, 15N resonance assignment of the full-length K-Ras bound to GDP. BioMagResBank. https://bmrb.io/data_library/summary/index.php?bmrbId=30825. Deposited 9 December 2020.
44. A. K. Sharma, A. E. Maciag, Solution structures of full-length K-RAS bound to GDP. Protein Data Bank. https://www.rcsb.org/structure/7KYZ. Deposited 9 December 2020.